Exploring the compatibility of phosphopantetheinyl transferases with acyl carrier proteins spanning type II polyketide synthase sequence space

Areta L. N. Bifendeh,[1] Kenneth K. Hsu,[1] Christina M. McBride,[1] Charlie M. Ferguson,[1] Eva R. Baumann,[2] Diego Capcha-Rodriguez,[2] Xinnuo Chen,[1] Berlensie Chery,[1] Margo M. Chihade,[1] Paola Delgado Umpierre,[1] Taliyah Evans,[2] Carolyn H. Everett,[1] Syeda F. Faheem,[2] Oscar D. Garrett,[2] Aliya R. Gottesfeld,[1] Ishir G. Gupta,[1] Jason D. Haas,[1] Theresa A. Haupt,[1] Jean Katz,[1] Sadie Kim,[1] Matthias Langer,[2] Vy Le,[1] Kevin K. Li,[1] Baldwin Zhao,[2] Siyue Lin,[2] Kelsey N. Mabry,[1] Anna Malkov,[1] Abigail T. Marquis,[1] Kieran R. McDonnell,[1] Kristen Min,[2] Nicholas B. Mostaghim,[1] Krysta M. Nichols,[1] Rebecca A. Osbaldeston,[2] Trisha T. Phan,[1] Alana T. Ponte,[1] Tala Qaraqe,[2] Bianca S. Rosas,[1] Caroline S. Smith,[1] Logan E. Smith,[1] Maisie W. Smith,[2] Aviva C.R. Soll,[2] Gabriel Rocco Sotero,[1] Isabel E. Thornberry,[1] Kristina Tran,[1] Quynh K. Vo,[1] Marcos G. Yoc-Bautista,[1] Madison Young,[2] Kelly A. Zukowski,[1] Robert Fairman,[2] Kimberly A. Wodzanowski,[2] Michael A. Herrera,[3,*] Yae In Cho,[1,^,*] Louise K. Charkoudian[1,*]

[1]Department of Chemistry, Haverford College, Haverford, PA 19041, USA

[2]Department of Biology, Haverford College, Haverford, PA 19041, USA

[3]School of Chemistry, The University of Edinburgh EH9 3FJ, UK

[^]Current address: Department of Chemistry and Biochemistry, Providence College, Providence, RI, 02918, USA

*Corresponding authors: Michael A. Herrera (mherrera@ed.ac.uk), Yae In Cho (ycho@providence.edu) and Louise K. Charkoudian (lcharkou@haverford.edu)

Keywords

phosphopantetheinyl transferase, acyl carrier protein, polyketide, synthase

One sentence summary

Seventeen acyl carrier proteins from diverse type II polyketide synthases were evaluated for their compatibility with three phosphopantetheinyl transferases; Results, along with sequence level-analyses and predictive structural modelling, reveal specific regions that can guide future strategic engineering efforts.

Abstract

Phosphopantetheinyl transferases (PPTases) play an essential role in primary and secondary metabolism. These enzymes facilitate the post-translational activation of acyl carrier proteins (ACPs) central to the biosynthesis of fatty acids and polyketides. Modulation of ACP-PPTase interactions is a promising approach to both increase access to desired molecular outputs and disrupt mechanisms associated with disease progression. However, such an approach requires understanding the molecular principles that govern ACP-PPTase interactions across diverse synthases. Through a multi-year, course-based undergraduate research experience (CURE), 17 ACPs representing a range of putative type II polyketide synthases, from actinobacterial and non-actinobacterial phyla, were evaluated as substrates for three PPTases (AcpS, Sfp, and vulPPT). The observed PPTase compatibility, sequence-level analyses, and predictive structural modelling suggest that ACP selectivity is driven by amino acids surrounding the conserved, modified serine on the ACP. We propose that vulPPT and Sfp are driven primarily by hydrophobic contacts, whereas AcpS may favor ACPs which exhibit high net-negative charge density, as well as a broad electronegative surface distribution. Furthermore, we report a plausible, hitherto unreported hydrophobic interaction between vulPPT and a conserved ACP crease, upstream of the invariant serine, which may facilitate docking. This work provides a catalog of compatible and incompatible ACP-

PPTase partnerships, highlighting specific regions on the ACP and/or PPTase that show promise for future strategic engineering and inhibitor development efforts.

Introduction

Phosphopantetheinyl transferases (PPTases) play a critical role in a range of metabolic pathways. These enzymes facilitate the post-translational activation of acyl carrier proteins (ACPs) in fatty acid synthases (FASs) and polyketide synthases (PKSs), as well as peptidyl carrier proteins (PCPs) in non-ribosomal peptide synthetases (NRPSs). ACPs and PCPs, which are considered central hubs of their synthase/synthetases, present as ~ 10 kDa helical bundles with a conserved serine at the *N*-terminus of helix II (Crosby & Crump, 2012). PPTases install an 18 Å, coenzyme-A (CoA) derived 4´-phosphopantetheine (Ppant) arm at the conserved serine site on the ACP/PCP, thereby converting the inactive *apo*-ACP/PCP to its active *holo* form (**Figure 1**). The terminal thiol of the protein-bound Ppant arm serves as a molecular tether to transport building blocks (*e.g.* malonyl CoA) and intermediates as thioesters during the multi-step assembly of a natural product.

Characterizing the interaction between ACPs and the PPTases that modulate their activity could increase access to medicinally relevant agents. For example, Sørensen and colleagues increased the *in vivo* production of target fungal polyketides with promising bioactivity by discovering ACP-PPTase partnerships that maximized natural product formation (Pedersen et al., 2022). Alternatively, inhibitors of PPTase-mediated activation could act as novel antimicrobial agents, as shown by Ballinger and colleagues through the identification of a small molecule that inhibit the PPTase crucial for the biosynthesis of mycobacterial structural and virulence lipids (Ballinger et al., 2019). Expanding the impact of such approaches requires an improved understanding of ACP-PPTase compatibility across a wide sequence space.

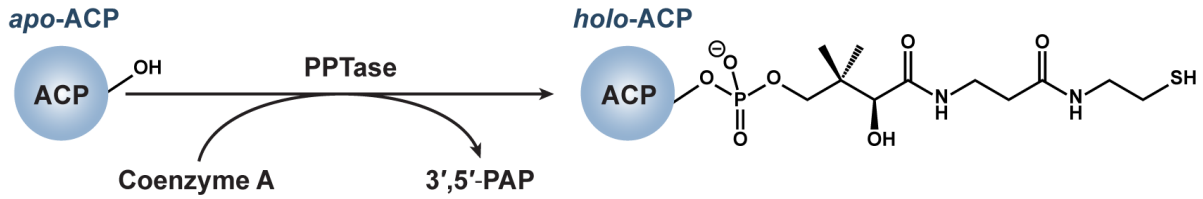

Figure 1. The PPTase-catalyzed conversion of an inactive "*apo*" ACP to the active "*holo*" ACP. *apo*-ACPs are activated to their *holo* form via the PPTase-catalyzed installation of

a coA-derived 4´-phosphopantetheine (Ppant) arm onto the conserved serine at the *N*-terminus of ACP helix II.

ACP structure and function are largely conserved across species. For example, ACPs from both type II PKS and FAS systems are discrete proteins that iteratively load malonyl CoA, present it to a cognate ketosynthase (KS) for a decarboxylative Claisen-like condensation reaction, then transfer the growing chain to other synthase components and/or back to the KS. In addition to this conserved role, ACPs engage in a suite of other protein-protein interactions (PPIs), as exemplified by the archetypical FAS ACP ("AcpP"), which interacts with >25 protein partners (Bartholow et al., 2021).

Despite having nearly identical roles in these systems, ACPs from type II PKSs typically cannot be interchanged with ACPs from type II FASs (Cho et al., 2022; Worthington et al., 2008, 2010; Ye & Williams, 2014). This phenomenon– where ACP function is highly conserved across PKSs, while ACP-partner compatibility is not – extends to ACP-PPTase interactions as well (Bräuer et al., 2020; Crosby & Crump, 2012; Cummings et al., 2019; Li et al., 2025; Pedersen et al., 2022). Historically, the PPTase from the *Escherichia coli* FAS system, AcpS (Lambalot & Walsh, 1995), and the PPTase from the *Bacillus subtilis* surfactin biosynthesis pathway, Sfp (Quadri et al., 1998; Sunbul et al., 2009), have been widely used in biosynthetic engineering efforts due to their broad substrate specificity. Yet, recent reports suggest that these "gold standard" promiscuous PPTases are not compatible with all ACPs, especially those from underexplored phyla (Bräuer et al., 2020; Li et al., 2025; Liu et al., 2020; Pedersen et al., 2022). While this incompatibility is a barrier to accessing ACPs in their *holo* state, it simultaneously offers a unique opportunity to explore the factors that govern ACP-PPTase interactions.

As part of a course-based undergraduate experience (CURE), 17 ACPs (**Tables S1** and **S2**) from phylogenetically diverse putative type II PKSs were surveyed for their compatibility with each of three PPTases – AcpS, Sfp (specifically the R4-4 mutant, engineered to increase substrate scope) (Sunbul et al., 2009), and a newly discovered PPTase from *Dictyobacter vulcani* (Hsu et al., 2025), which is referred to as vulPPT in the present manuscript. The data herein support that the interaction between ACP and PPTases is driven by specific protein-protein interactions. Using the data from this panel enabled us to infer the role of specific ACP sequence motifs and physicochemistry in determining ACP-PPTase compatibility.

The impact of this work is three-fold. First, this work was carried out through CUREs, exposing 47 students to the exciting field of natural product biosynthesis, enabling them to learn foundational concepts and techniques of biochemistry while contributing to the field. Second, conclusions drawn from these studies can guide the selection of the optimal PPTase to activate ACPs from different sources, thereby supporting combinatorial biosynthesis efforts. Third, our molecular-level insights can be used to develop more specific ACP-PPTase inhibitors for antimicrobial applications and/or engineer ACPs/PPTases to confer compatibility and improve synthase output.

Materials and Methods

Protein expression and purification. In pairs, students enrolled in the CURE identified and worked on a single target ACP. Plasmids were constructed and transformed into *E. coli* BL21(DE3) cells as outlined in Supplementary Data.

A single colony of *E. coli* BL21(DE3) transformed with the target plasmid was used to inoculate 10 mL of LB medium supplemented with 50 µg/mL kanamycin. The culture was incubated at 37 °C with shaking at 200 rpm for 12–18 hours. This 10-mL seed culture was then used to inoculate 1-L LB medium with 50 µg/mL kanamycin, which was grown at 37 °C, 200 rpm in a shaking incubator until the optical density at 600 nm (OD_{600}) reached 0.4–0.6. This production culture was induced by adding isopropyl-β-D-thiogalactoside (IPTG) to a final concentration of 250 µM, and the culture was incubated overnight (~18 hours) at 18 °C with shaking at 200 rpm. Cells were harvested by centrifugation (Beckman Coulter Avanti J-E High-Speed Centrifuge, JA-10 rotor, 6,000 rpm, 4 °C, 20 min). Cell pellets were transferred to a 50-mL conical tube and stored at –80 °C until purification.

The expressed cell pellet from a 1-L expression culture was resuspended with 20–30 mL of ice-cold lysis buffer (50 mM sodium phosphate buffer, 300 mM NaCl, 10 mM imidazole, 10% (v/v) glycerol, pH 7.6). Cell lysis was performed on ice using an XL-200 Microson ultrasonicator at 40% amplitude with 30 sec on/30 sec off cycles for 10 minutes or longer, until the lysate became visibly more translucent. The lysate was centrifuged (Beckman Coulter Avanti J-E High-Speed Centrifuge, JA-18, 13,000 rpm, 4 °C, 1 hour). The resulting supernatant was transferred into a 50-mL conical tube and incubated with 1 mL of pre-equilibrated Ni-NTA resin (GoldBio). The mixture was gently nutated at 4 °C for at least 1.5 hours to allow protein binding to resin before transferring to an Econo-Pac gravity flow column (Bio-Rad). After collecting the flow-through, the resin was washed sequentially with ~20 mL of the lysis buffer, followed by the addition of wash buffer (50 mM sodium phosphate buffer, 300 mM NaCl, 30 mM imidazole, 10% (v/v) glycerol, pH 7.6) until the $A_{280} < 0.05$ (~50 mL). Protein elution was performed using elution buffer (50 mM sodium phosphate buffer, 100 mM NaCl, 250 mM imidazole, 10% (v/v) glycerol, pH 7.6) and 10 x 1-mL elution fractions were collected. Protein concentration of each fraction was determined by Nanodrop 2000 spectrophotometer (Thermo Fisher Scientific), and the fractions with $A_{280} > 0.15$ and $A_{260}/A_{280} < 1.00$ were pooled, aliquoted, flash-frozen with liquid N_2, and stored at –80 °C. The concentration of purified proteins was determined using the bicinchoninic acid (BCA) assay. Purified proteins were characterized by SDS-PAGE (**Figure S1**) and LC-MS (**Figure S3**).

ACP-PPTase Phosphopantetheinylation Assay

Each *apo*-ACP was reacted with each of the three PPTases (Sfp R4-4, AcpS, and vulPPT) by combining the following components in a 1.5-mL microfuge tube to achieve the final concentrations indicated in 100 µL total volume: ACP (80 µM), 50 mM sodium phosphate buffer, pH 7.6, dithiothreitol (DTT) (2.5 mM, from 1 M stock), $MgCl_2$ (10 mM, from 250 mM stock), coenzyme A (0.8 mM, from 50 mM stock), and PPTase (1 µM, added last to initiate the reaction). Reactions were incubated at room temperature with gentle shaking on an orbital shaker for 18 hours. At the 18-hour mark, 50 µL of the reaction mixture was removed and quenched by adding 10 µL of 25% (v/v) formic acid. All experiments were repeated in triplicate by a senior undergraduate thesis student to increase experimental rigor and ensure reliability of results.

Liquid Chromatography-Mass Spectrometry (LC-MS)

ACP samples were analyzed using an Agilent InfinityLab G6125B LC-MS system coupled with an Agilent 1260 Infinity II LC, fitted with a Waters XBridge Protein BEH C4 reverse phase column (300 Å, 3.55 µm, 2.1 mm × 50 mm) and an XBridge Protein BEH C4 Sentry guard cartridge (300 Å, 3.5 µm, 2.1 mm × 10 mm). The column temperature was maintained at 45 °C during liquid chromatography. Mass spectra were acquired using electrospray ionization mass spectrometry (ESI-MS) in positive mode. Two LC-MS grade solvent sources were used: Solvent A (H_2O + 0.1% (v/v) formic acid) and Solvent B (acetonitrile + 0.1% (v/v) formic acid).

For post-purification confirmation of apo-ACP starting material: Samples were prepared by diluting 10 µL of *apo*-ACP with 90 µL of LC-MS grade water. The following solvent gradient was used after 20 µL injection of the sample: 0–1 min, held at 5% B; 3.1–4.52 min, 5%→ 95% B; 4.52–4.92 min, 95% → 5% B, and 4.92–9 min held at 5% B. The flow rate was maintained at 0.4 mL/min, with ESI-MS parameters set to a capillary voltage of 3000 V and a fragmentation voltage of 75 V.

For apo/holo quantification after phosphopantetheinylation assay: Quenched reactions (50 µL of the reaction mixture + 10 µL of 25% (v/v) formic acid) were neutralized and diluted by sequentially adding 20 µL of 5% (v/v) NaOH and 20 µL of LC-MS grade water, yielding a final volume of 100 µL. Before sample injection, the column was first equilibrated for 10 min at 10% B. A 20 µL injection was followed by the following solvent gradient: 0–5 min, 10% → 30% B; 5–40 min, 30% → 50% B; 40–45 min, 50% → 95% B; 45–46 min, held at 95% B; 46–51 min, 95% → 10% B; and 51–62 min, held at 10% B. The flow rate was maintained at 0.4 mL/min, and ESI-MS was conducted using the same ionization parameters as above.

Acquired mass spectra were deconvoluted using ESIprot online (Winkler, 2010). The resulting molecular weights (MWs) were compared to the theoretical MWs to verify successful phosphopantetheinylation. For *apo/holo* quantification, LC chromatograms at 280 nm absorbance were baseline-corrected, and the area under the curve for each *apo*- and *holo*-ACP peak was used to calculate their relative abundance in Microsoft Excel. All LC-MS and LC chromatograms were plotted using Origin 2023b.

Sequence analysis, predictive structural modelling and molecular dynamics simulation. The nucleotide accession number for each ACP which underwent less than 98% *holo* conversion with at least one tested PPTase was input into the antiSMASH (Blin et al., 2023). The corresponding PPTase for bweACP was omitted, as the corresponding genome in NCBI was unannotated (bweACP) and thus could not be easily searched using antiSMASH. The type II PKSs containing the ACPs were searched for genes annotated as a “holo-(acyl-carrier-protein) synthase” or “4’-phosphopantetheinyltransferase.” A corresponding PPTase for dacACP was not annotated in the cluster and was thus omitted. The relevant protein sequences were retained, and the accession numbers were searched in NCBI for annotation of predicted PPTase type (Sfp vs. AcpS). Multiple sequence alignments (MSAs) were performed using Clustal Omega (EMBL-EBI,

European Molecular Biology Laboratory-European Bioinformatics Institute) (Madeira et al., 2024), and visualised in ESPript 3 (Robert & Gouet, 2014). Sequence net charges were computed using Isoelectric Point Calculator 2.0 (Kozlowski, 2021). All structural predictions were performed using AlphaFold3 (via AlphaFold server) (Abramson et al., 2024) Simulations were performed using GROMACS 2021 (Abraham et al., 2015). Protein charges were computed using CHARMM36 all-atom forcefield (Huang & MacKerell, A. D., 2013). Models were solvated in TIP3P water in a cubic box, and the net protein charge was counterbalanced using simulated sodium/chloride ions. The system was energy-minimized by sequential steepest descent/conjugate gradient descent and equilibrated to 300 K and 1 bar using V-Rescale thermostat/Berendsen barostat. Following a 10 ns (1 x10^8 time steps) production MD, the trajectory was re-centered with additional rotational and translational fitting. UCSF Chimera v1.18 (Pettersen et al., 2004) was used for trajectory visualization and ensemble clustering. General model viewing and analysis was performed using ChimeraX v1.8 (Pettersen et al., 2021) and PyMOL 3.0.4.

Results and Discussion

Diversity of Selected ACP Candidates

Target ACPs were selected to represent a range of putative type II PKSs from the well-studied actinobacterial and the largely uncharacterized group of non-actinobacterial phyla (**Figure 2** and **Tables S1 and S2**) (McBride et al., 2023). ACPs with variations in the region flanking the conserved serine were prioritized. To further narrow down ACPs to incorporate into the CURE, we selected those that came from an organism residing in an intriguing environment that might stimulate student curiosity. For example, vulACP originates from *Dictyobacter vulcani* isolated from a volcano in Japan (Zheng et al., 2020), and zooACP originates from *Zooshikella harenae* sp WH53 isolated from Pacific oysters (Pira et al., 2021). The ACPs selected show broad sequence-level diversity, ranging from 8.11-83.3% identity with a median of 20.3%. From MSAs, the selected actinobacterial ACPs show moderate sequence identity with other ACPs from the same phylum (46.7 ± 13.2%, **Figure 2B-C**). In contrast, the selected non-actinobacterial ACPs are more diverse, both within their own phylum (24.0 ± 5.16%) and compared to our actinomycete ACPs (16.9 ± 3.46%, **Figure 2B-C**). Collectively, these candidates cover a wide area of the type II ACP sequence space. Therefore, we anticipated an array of PPTase compatibilities useful for developing sequence-function hypotheses.

E. coli serves as a heterologous host for robust expression of ACPs from diverse phyla

All 17 ACPs chosen were expressed in *E. coli* BL21(DE3) cells with an *N*-terminal His_6-tag and were subsequently purified via Ni-NTA affinity chromatography with yields ranging from 5 – 26 mg per liter culture. The observed yields demonstrate the robustness of a single expression/purification protocol to obtain a diverse set of ACPs. The ACPs were expressed primarily in their *apo* form with their SDS-PAGE migration patterns in alignment with their ~ 10 kDa molecular weights under both reducing and non-reducing

conditions (**Figure S1 – S3**). The observed migration patterns are consistent with other type II PKS ACPs and in contrast to the *E. coli* AcpP, which migrates at a higher-than-expected molecular weight, attributed to its unique charge distribution (Garwin et al., 1980).

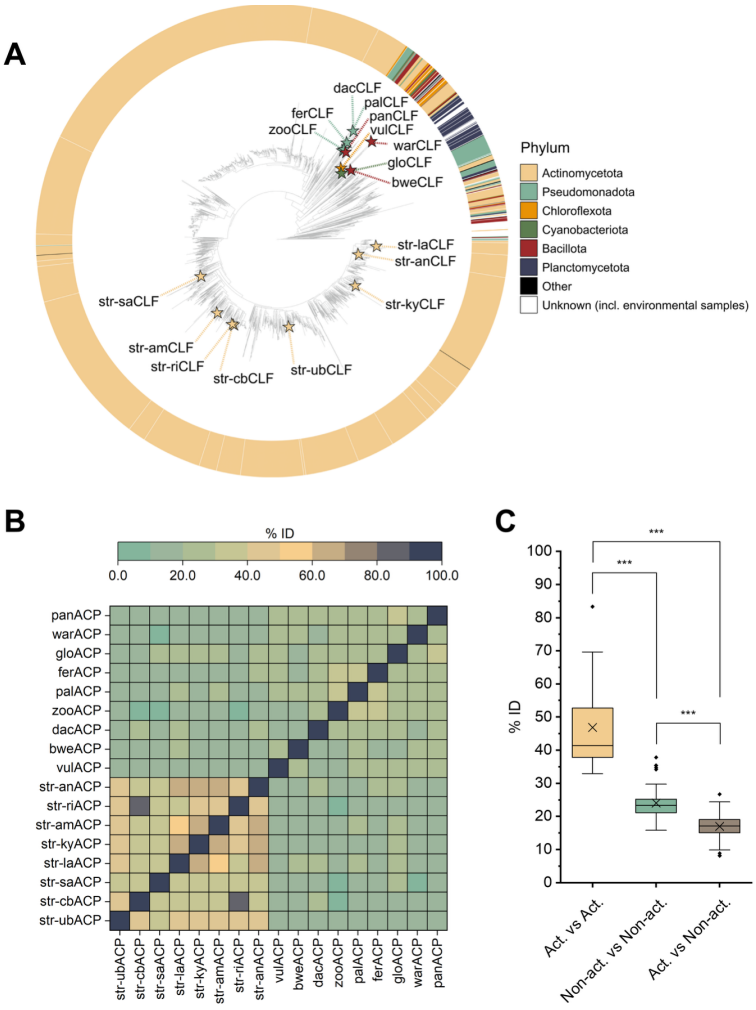

Figure 2. The type II PKS ACPs addressed in this study belong to phylogenetically diverse BGCs. (A) The featured phylogenetic tree represents 6,322 type II PKS chain length factor (CLF) protein sequences identified in our previous global bioinformatic analysis of type II PKS BGCs. For methods associated with the construction of the tree, see McBride et al. (2023). The ring signifies the phylum classification for each terminal node. Cognate CLFs for the ACPs explored in this study are marked with a star. **(B)** Pairwise percent sequence identity (%ID) heatmap between all actinobacterial and non-actinobacterial ACPs selected for study. **(C)** Box plot showing the distribution and central tendency of ACP %IDs, both within and between the actinobacterial (act) and non-actinobacterial (non-act) phyla. Boxes represent the interquartile range (IQR). Whiskers extend to data points up to 1.5 x the IQR from the lower and upper quartiles. Median values are shown as black bands, means are shown and black crosses. (***) = $p \leq 0.001$ (Welch's ANOVA with Games-Howell post-hoc test).

PPTases demonstrate preference for actinobacterial ACPs over non-actinobacterial ACPs.

The conversion of ACPs from their *apo* to *holo* form was monitored by a +340 Da change in mass corresponding to the installation of the Ppant arm. Analysis via single quadrupole LC-MS, resulted in each ACP displaying a set of ~10 m/z peaks within the 650-1400 Da range corresponding to the +9 to + 18 charge states, which can be deconvoluted using ESIprot (Winkler, 2010) to establish the molecular weight of the ACP.

Optimization of LC-MS methods using our set of 17 ACPs led to a method that could effectively separate the *apo* and *holo* forms of most ACPs by LC. Peak boundaries were determined by coupling UV absorbance with the MS data at each time point: integration ranges were defined based on reproducible retention behavior across replicates and confirmed by MS identity to ensure that each region corresponds to a single ACP species; the area under the curve(s) was then used to determine the relative percent of each ACP in the *apo* versus *holo* form after reaction with each PPTase. ACPs in their *apo* form typically eluted later than those in their *holo* form (**Figures S4-S20**). The broadened and/or heterogenous peaks observed in the ACP LC traces reflect the established conformational heterogeneity and flexibility of ACPs (Wang et al., 2016; Sztain et al., 2021; Nguyen et al., 2014; Purcell et al., 1999).

The three PPTases explored (Sfp, AcpS, and vulPPT) show varied preferences for ACP substrates; notably, all three PPTases phosphopantetheinylate the actinobacterial ACPs (**Figure 3, top panel**). In fact, of the eight actinobacterial ACPs explored, only one ACP-PPTase pairing (str-amACP-Sfp) demonstrated less than 50% conversion. Four ACPs (str-ubACP, str-cbACP, str-saACP, str-laACP) were fully or near-fully phosphopantetheinylated with all three PPTases. In contrast, ACP-PPTase compatibility was less commonly observed in the non-actinobacterial group (**Figure 3, bottom panel).** Of the nine non-actinobacterial ACPs explored, only one ACP from the non-actinobacterial group (vulACP) was phosphopantetheinylated with all three PPTases. While bweACP and dacACP were fully converted to their *holo* forms by one (dacACP-AcpS) or two (bweACP-Sfp and bweACP-vvulPPT) PPTases, others in this group were not converted to a majority *holo* state by any of the three PPTases. Two ACPs (zooACP and palACP) showed low-level (~2-4%) activation with AcpS, and vulPPT was able to convert zooACP to 17% *holo* state under the conditions studied. The remainder of the ACP-PPTase partnerships studied in this group were deemed non-compatible, with no conversion observed. It is possible that modifying the conditions (*e.g.,* temperature) could improve conversion rates, as has been observed previously (Hsu et al., 2025).

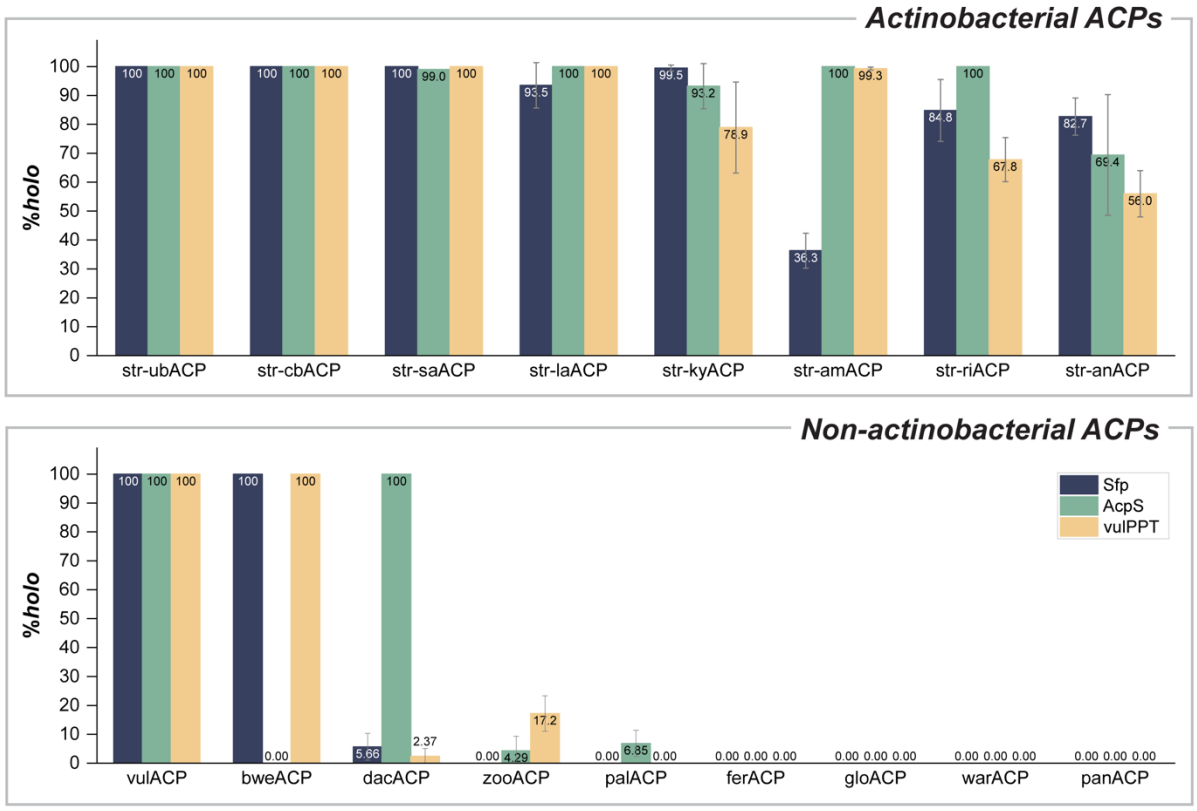

Figure 3. Sfp, AcpS and vulPPT demonstrate broader substrate scope within the actinobacterial ACPs (top) than non-actinobacterial ACPs explored (bottom). The % *holo* was calculated based on the ratio of the area under the curve for the Abs_{280} peak in the LC trace corresponding to *holo* versus the total area under the curve for the Abs_{280} peaks in the LC trace corresponding to total ACP and multiplying by 100. The bar height represents the average % *holo* for the ACP-PPTase pair evaluated in triplicate, with error bars representing the standard deviation. All reactions were run at room temperature for 18 hours under the following conditions: ACP (80 μM), DTT (2.5 mM, from 1 M stock), $MgCl_2$ (10 mM, from 250 mM stock), coenzyme A (0.8 mM, from 50 mM stock), PPTase (1 μM) in 50 mM sodium phosphate buffer, pH 7.6. Full names of each ACP and their corresponding sequence can be found in Supplementary Data (**Tables S1** and **S2**) along with the LC-MS results for each phosphopantetheinylation reaction.

Sequence Analysis and Structural Modelling

To complement our experimental analyses, we generated structural models of each PPTase (AcpS, vulPPT, Sfp) docked with their respective cognate carrier proteins (**Figure 4**). Alongside available crystal structures (PDB: 4MRT, 5VCB) and primary sequence analyses (**Figure S21**), we aimed to rationalize the influence of ACP sequence motifs, and physicochemistry on PPIs with our selected PPTases. This analysis may help to elucidate the differential *apo*-to-*holo* conversion efficiencies amongst actinobacterial and non-actinobacterial ACPs. Each structure was generated using AlphaFold3 (Abramson et al., 2024) and relaxed in a very brief (10 ns) molecular dynamics simulation,

from which frames were clustered and extracted to study PPIs. MSA of all ACPs was used to identify sequence motifs (and deviations therein), and structural models were analyzed using a suite of molecular visualization tools in ChimeraX (Pettersen et al., 2021).

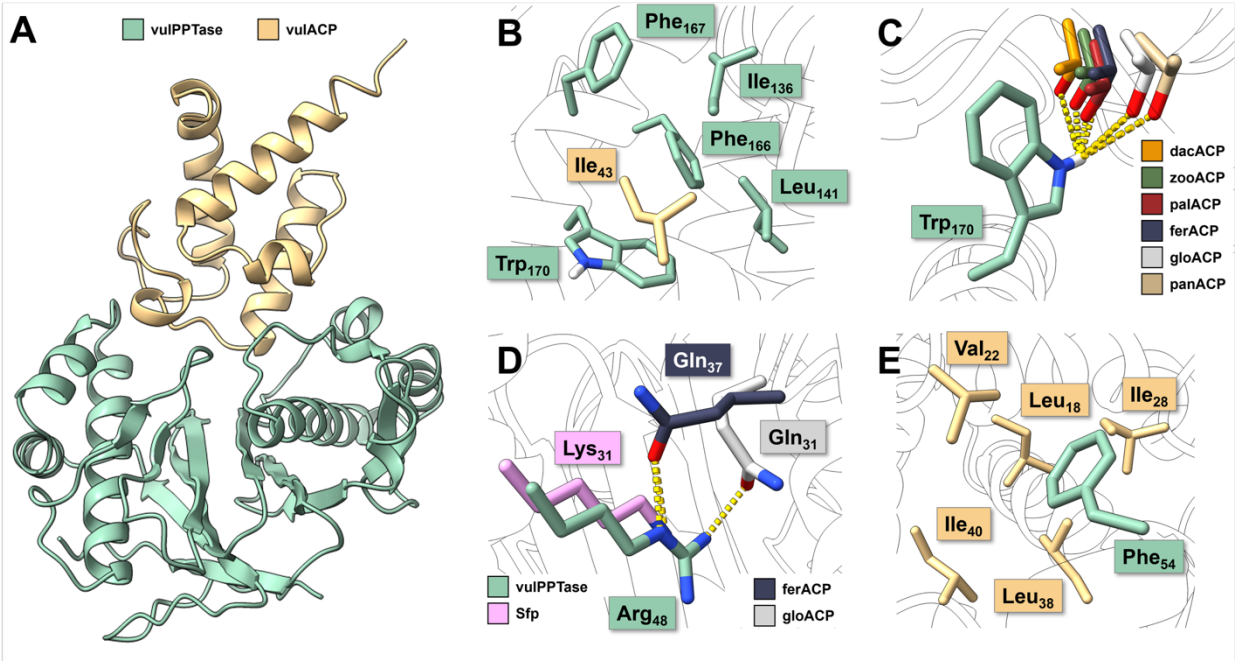

Figure 4. Predictive structural modelling of vulPPT with cognate and non-cognate ACPs. (A) Predicted vulPPT-vulACP complex (predicted TM score = 0.89) following relaxation by molecular dynamics simulation. **(B)** vulACP Ile43 buried in a conserved vulPPT hydrophobic pocket. **(C)** Structural alignment of non-cognate, non-actinobacterial ACPs carrying a (Ile/Leu)→Thr variation, and a possible hydrogen-bonded contact with vulPPT Trp_{170}. **(D)** Plausible hydrogen-bonded contacts between ferACP Gln_{37}/gloACP Gln_{31} and Sfp Lys_{31}/vulPPT Arg_{48}. **(E)** Plausible hydrophobic interactions between vulPPT Phe_{54} and a conserved vulACP hydrophobic crease.

Analysis of the predicted vulPPT-vulACP complex (predicted TM-score = 0.89; **Figure 4A**) revealed an extensive hydrophobic binding pocket in vulPPT (**Figure 4B**). This pocket is sculpted by Ile_{136}, Leu_{140} and aromatic residues (Phe_{146}, Phe_{166}, Phe_{167}, Trp_{170}). Together, these residues accommodate Ile_{43} on vulACP, which lies directly *C*-terminal of the invariant, modifiable Ser (Ser_{42}). The architecture of this pocket resembles that of Sfp (Tufar et al., 2014), whose cognate surfactin PCP partners harbour a Ile→Leu variation at this equivalent position. Previously, we demonstrated by NMR titration experiments that ACPs carrying a Leu→Thr variation cannot undergo *apo*-to-*holo* conversion using Sfp, due to increased binding affinity that impedes complex dissociation (Li et al., 2025). Following *in silico* mutagenesis of vulACP Ile_{43}, we hypothesize that the Thr hydroxyl group may form a hydrogen-bond with the indole moiety of vulPPT Trp_{170}, or its equivalent Trp_{147} in Sfp (**Figure S22**). Of note, six of the studied non-actinobacterial ACPs carry a

Thr at this equivalent position (dac/zoo/pal/fer/glo/war/panACP). Our experimental data show that these ACPs either were not modified or underwent minimal conversion using vulPPT/Sfp (**Figure 3**). *In silico* replacement of vulACP with these non-actinobacterial ACPs (by structural alignment; **Figure 4C**) places their respective Thr residues within plausible hydrogen-bonding distance to vulPPT Trp_{170}. Together with our prior NMR data, we propose that the additional hydrogen-bond afforded by (Leu/Ile)→Thr substitution may over-stabilize the ACP-vulPPT/Sfp complex, thus impeding productive turnover of *holo*-ACP.

We further propose a key role for vulACP Gly_{39} in minimizing steric clashes with vulPPT. In actinomycete ACPs, Gly at this position is tightly conserved as part of the GY(D/E)SL motif. We hypothesize that deviations from Gly may hamper productive engagement and dissociation of the ACP-PPTase complex. For instance, we have previously observed by NMR how Gly → Gln variants (as seen in fer/gloACP) form tighter complexes with Sfp (Li et al., 2025). From our modelling data, we propose that this could arise due to hydrogen-bonding with Sfp Lys_{31}, a contact which could plausibly occur with vulPPT Arg_{48} (**Figure 4D**). Further variations may result in steric clashes (war/zooACP) or electrostatic effects (palACP), albeit the precise mechanisms have yet to be studied.

Distinctly from Sfp, vulPPT may exploit a hydrophobic crease on vulACP, formed by the loop connecting helices αI and αII. In our model, Phe_{54} in vulPPT (Cα pLDDT = 90.2) is buried by Leu_{18}, Val_{22}, Ile_{28}, Leu_{38}, Gly_{39} and Ile_{40} of vulACP (mean Cα pLDDT = 85.8; **Figure 4E**). Of note, Phe_{54} is located on the joint of a helix-turn-helix in vulPPT. By comparison, the connecting "turn" is shorter in Sfp due to the deletion of this equivalent Phe_{54} position, which may prevent deeper engagement with this ACP crease. Furthermore, through vulACP-Sfp docking (predicted TM score = 0.87) and simulation, we observed that Sfp Tyr_{36} engages in hydrogen-bonding with vulACP Asp_{26}, further impeding access to this hydrophobic crease (**Figure S23**). By structural alignment with vulACP, we observed that all ACPs studied could, in principle, accommodate vulPPT Phe_{54} via similar hydrophobic interactions, and subtle variations in this pocket may give rise to different conversion efficiencies. Furthermore, the cognate vulACP-vulPPT complex may benefit from additional stabilizing contacts, including a salt bridge between vulPPT Arg_{51} and vulACP Asp_{37}, as well as a H-bond between vulPPT Tyr_{53} and vulACP Glu_{27} and Asp_{37}. These interactions may serve an additional role to "pull" the ACP loop over vulPPT Phe_{54}, further burying it within the crease (**Figure S24**).

Taken all together, we find that ACPs that are compatible with both vulPPT and Sfp share the motif G*x*(D/E)S(I/L), where x is Tyr or an equivalent hydrophobic residue. In conjunction with our previous NMR studies, we propose that Gly and Leu/Ile in the G*x*(D/E)S(I/L) motif modulate the dynamics of ACP-Sfp and ACP-vulPPT interactions by mitigating sidechain-sidechain clashes and minimizing overly stabilizing hydrogen-bonding. Furthermore, the hydrophobic residue *x* may facilitate docking with vulPPT by helping to bury Phe_{54}, which is unique to vulPPT, within the binding interface. The present model lays the foundation for future crystallographic and mutagenesis studies.

In contrast, AcpS-ACP compatibility seems to be governed by a distinct set of non-covalent interactions. The *E. coli* AcpP–AcpS docking interface is more extensive and governed primarily by electrostatics (Marcella et al., 2017). The electropositive binding surface of AcpS (**Figure 5A**) is composed of several Arg residues ($Arg_{15/22/26/29/30/69/115}$), which can form numerous salt bridges with the highly acidic AcpP. Like Sfp/vulPPT, additional hydrophobic contacts involving AcpS (Val_{11}, Ile_{16}, Val_{19}, Leu_{27}, Val_{31}, Leu_{50}, Phe_{54}, Phe_{74}) and AcpP helix αII (Leu_{38}, Val_{41}, Met_{45}) further contribute to the binding interface (**Figure S25**). Due to the complexity of this interaction surface, it remains difficult to predict specific residue variations (or combinations thereof) that could impede *apo*-to-*holo* conversion. Interestingly, we revealed by isoelectric point prediction (Kozlowski, 2021) that ACPs which performed well with AcpS (>60% post-translational modification) exhibit significantly greater negative net charge at pH 7.4 (–14.1 ± 1.44, $n = 10$), compared to ACPs which performed poorly (–6.93 ± 2.64, $n = 7$, $p = 3.11 \times 10^{-4}$; **Figure 5B**). Electrostatic potential surface maps (**Figure 5C**) further indicate that both the magnitude and spatial distribution of negative charge are potential predictors of AcpS compatibility. Notably, all actinobacterial ACPs (alongside dac/vulACP) present extensive electronegative surfaces that closely resemble AcpP **(Figure 5C and S26**). These observations suggest that effective AcpS recognition relies on an AcpP-like electrostatic presentation, supported by hydrophobic contacts on helix αII, to drive productive engagement and post-translational modification with AcpS. Future studies are needed to determine whether AcpS compatibility can be engineered into non-cognate ACPs via the strategic incorporation of acidic residues.

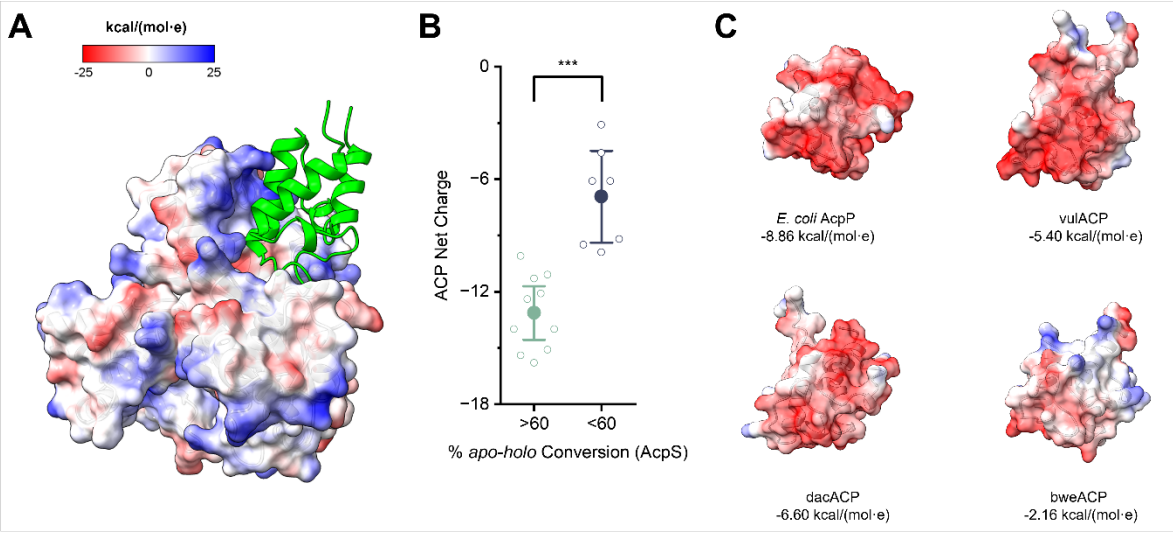

Figure 5. Electrostatic rationale for AcpS-ACP interaction. (A) Reconstructed *E. coli* AcpP-AcpS complex (PDB: 5VCB). The electrostatic surface potential map of AcpS is shown. *E. coli* AcpP is depicted in lime green. **(B)** ACP net charge comparison between ACPs showing strong (>60% conversion) and poor (<60% conversion) compatibility with AcpS. Error bars represent 95% confidence interval. (***) = $p \leq 0.001$ (Welch two-sample t-test). **(C)** Electrostatic surface potential maps of *E. coli* AcpP and non-actinobacterial

ACPs vul/dac/bweACP. All ACPs are rendered in the same orientation. Color map is identical to panel (A). Mean electrostatic potentials (kcal/(mol·e)) are shown.

The four ACPs that were not activated by any of the three PPTases studied (ferACP, gloACP, warACP and panACP) and the two that were minimally activated (zooACP and palACP) each originate from BGCs harboring a gene annotated as encoding for a '*holo*-acyl carrier protein synthase' or '4´-phosphopantetheinyl transferase' (**Figure S27**). It is unclear at this time whether there are features of these PPTases that make them uniquely suited to activating their cognate ACPs. In the case of gloACP, the putative cognate PPTase did not convert *apo*-gloACP to *holo*-*glo*ACP under the traditional conditions studied, suggesting yet-to-be realized factors may be at play (Li et al., 2025).

Conclusions

The ACP-PPTase interaction is an ideal target for the development of new therapeutics given its central role in modulating both primary and secondary metabolism. Here, we catalog the ACP-PPTase compatibility of 17 diverse ACPs with three PPTases: AcpS, Sfp, and vulPPT. We find that actinomycete-derived ACPs, which show moderate sequence identity with one another, are more readily activated by the PPTases explored in this study, as compared with the non-actinobacterial ACPs that represent a larger sequence space. While previous studies highlight the role of amino acids *C*-terminal to the conserved ACP serine in PPTase compatibility, our work suggests that the identity of the amino acids *N*-terminal to this site also direct ACP-PPTase functional interactions. Through structural modelling, we speculate that specific hydrophobic and hydrogen bonding interactions, as well as steric clashes modulate the functional interactions between ACPs with Sfp and vulPPT, whereas more general electrostatic interactions guide ACP-AcpS compatibility. The highly tuned balance between ACP-PPTase complex formation and disassociation required for compatibility suggests that mutations that alter these non-covalent interactions will lead to changes in the ability of the PPTase to phosphopantetheinylate the ACP. We remain intrigued by those ACPs that are not activated by any of the three PPTases studied, and raise questions about whether these ACPs can be natively activated by their putative cognate PPTases. Future work will systematically evaluate inferences made from the current work to deepen our understanding of the molecular ground rules that govern ACP-PPTase interplay. Important unanswered questions of the field that are notably amenable to CUREs include "what is the role of Phe54 (vulPPT) in guiding ACP compatibility?", "Can the putative cognate PPTases activate those ACPs that were not activated by Sfp, AcpS and vulPPT?", "Why is str-amACP a better substrate for vulPPT than Sfp"?, and "how does the charge/size/polarity of amino acids upstream from the invariant Ser direct ACP folding and ability to be modified by PPTases?" Answers to these foundational questions can be applied to benefit human health by increasing access to natural products and inhibiting the virulence factors of common pathogens.

Acknowledgements

We would like to thank Haverford College for supporting the integration of research and teaching. We are grateful to Nicole Cunningham, Dr. Angus Unruh and Dr. Zak Kerrigan

for their support with media preparation and instrument maintenance/training. We are grateful to Yarra Ellett and Anna-Lee Thompson for helpful discussions.

Supplemental Information

Detailed experimental protocols, ACP names and sequences, SDS-PAGE data and LC-MS spectra are available in the accompanying Supplemental Information.

Author Contributions

L.K.C., Y.I.C., R.F. and K.A.W. designed and taught the course-based undergraduate experiences (CURE) with support of T.T.P., B.Z., C.M.M., C.M.F., and N.B.M. The following authors contributed to the manuscript through a CURE that involved experimental design, conducting experiments, analyzing data and contributing to the writing/review of this manuscript: C.M.M., E.R.B., D.C.R., X.C., B.C., M.M.C., P.D.U., T.E., C.H.E., S.F.F., O.D.G., A.R.G., I.G.G., J.D.H., T.A.H., J.K., S.K., M.L., V.L., K.K.L., S.L., K.N.M., A.M., A.T.M., K.R.M., K.M., N.B.M., K.M.N., R.A.O., T.T.P., A.T.P., T.Q., B.S.R., C.S.S., L.E.S., B.W.S., A.C.R.S., G.R.S., I.E.T., K.T., Q.K.V., M.G.Y-B., M.Y., K.A.Z. In addition, A.L.N.B., K.K.H., C.M.M., C.M.F., and Y.I.C. expanded and vetted the data set. M.A.H. conducted structural and sequence-based analyses. L.K.C., Y.I.C., C.M.M., A.L.N.B. and M.A.H. wrote the manuscript.

Funding

We are thankful to Haverford College and the National Science Foundation (CHE-2201984) for funding and supporting this project. C.M.M. was supported by a Beckman and Goldwater Scholarship.

Conflict of Interest

The authors declare no conflict of interest.

Data Availability

Data available upon request.

References

Abraham, M. J., Murtola, T., Schulz, R., Páll, S., Smith, J. C., Hess, B., & Lindahl, E. (2015). GROMACS: High performance molecular simulations through multi-level parallelism from laptops to supercomputers. *SoftwareX*, *1–2*, 19–25. https://doi.org/10.1016/j.softx.2015.06.001

Abramson, J., Adler, J., Dunger, J., Evans, R., Green, T., Pritzel, A., Ronneberger, O., Willmore, L., Ballard, A. J., Bambrick, J., Bodenstein, S. W., Evans, D. A., Hung, C.-C., O'Neill, M., Reiman, D., Tunyasuvunakool, K., Wu, Z., Žemgulytė, A., Arvaniti, E., … Jumper, J. M. (2024). Accurate structure prediction of biomolecular interactions with AlphaFold 3. *Nature*, *630*(8016), Article 8016. https://doi.org/10.1038/s41586-024-07487-w

Ballinger, E., Mosior, J., Hartman, T., Burns-Huang, K., Gold, B., Morris, R., Goullieux, L., Blanc, I., Vaubourgeix, J., Lagrange, S., Fraisse, L., Sans, S., Couturier, C., Bacqué, E., Rhee, K., Scarry, S. M., Aubé, J., Yang, G., Ouerfelli, O., … Nathan, C. (2019). Opposing reactions in coenzyme A metabolism sensitize *Mycobacterium tuberculosis* to enzyme inhibition. *Science*, *363*(6426), eaau8959. https://doi.org/10.1126/science.aau8959

Bartholow, T. G., Sztain, T., Patel, A., Lee, D. J., Young, M. A., Abagyan, R., & Burkart, M. D. (2021). Elucidation of transient protein-protein interactions within carrier protein-dependent biosynthesis. *Communications Biology*, *4*(1), 340. https://doi.org/10.1038/s42003-021-01838-3

Blin, K., Shaw, S., Augustijn, H. E., Reitz, Z. L., Biermann, F., Alanjary, M., Fetter, A., Terlouw, B. R., Metcalf, W. W., Helfrich, E. J. N., van Wezel, G. P., Medema, M. H., & Weber, T. (2023). antiSMASH 7.0: New and improved predictions for detection, regulation, chemical structures and visualisation. *Nucleic Acids Research*, *51*(W1), Article W1. https://doi.org/10.1093/nar/gkad344

Bräuer, A., Zhou, Q., Grammbitter, G. L. C., Schmalhofer, M., Rühl, M., Kaila, V. R. I., Bode, H. B., & Groll, M. (2020). Structural snapshots of the minimal PKS system responsible for octaketide biosynthesis. *Nature Chemistry*, *12*(8), 755–763. https://doi.org/10.1038/s41557-020-0491-7

Cho, Y. I., Armstrong, C. L., Sulpizio, A., Acheampong, K. K., Banks, K. N., Bardhan, O., Churchill, S. J., Connolly-Sporing, A. E., Crawford, C. E. W., Cruz Parrilla, P. L., Curtis, S. M., De La Ossa, L. M., Epstein, S. C., Farrehi, C. J., Hamrick, G. S., Hillegas, W. J., Kang, A., Laxton, O. C., Ling, J., … Charkoudian, L. K. (2022). Engineered Chimeras Unveil Swappable Modular Features of Fatty Acid and Polyketide Synthase Acyl Carrier Proteins. *Biochemistry*, *61*(4), 217–227. https://doi.org/10.1021/acs.biochem.1c00798

Crosby, J., & Crump, M. P. (2012). The structural role of the carrier protein – active controller or passive carrier. *Natural Product Reports*, *29*(10), 1111–1111. https://doi.org/10.1039/c2np20062g

Cummings, M., Peters, A. D., Whitehead, G. F. S., Menon, B. R. K., Micklefield, J., Webb, S. J., & Takano, E. (2019). Assembling a plug-and-play production line for combinatorial biosynthesis of aromatic polyketides in Escherichia coli. *PLoS Biology*, *17*(7), Article 7. https://doi.org/10.1371/journal.pbio.3000347

Garwin, J. L., Klages, A. L., & Cronan, J. E. (1980). Structural, enzymatic, and genetic studies of β-ketoacyl-acyl carrier protein synthases I and II of Escherichia coli. *Journal of Biological Chemistry*, *255*(24), 11949–11956.

Hsu, K. K., Ferguson, C. M., McBride, C. M., Mostaghim, N. B., Mabry, K. N., Fairman, R., Cho, Y. I., & Charkoudian, L. K. (2025). *A Phosphopantetheinyl Transferase from* Dictyobacter vulcani *sp. W12 Expands the Combinatorial Biosynthetic Toolkit*. https://doi.org/10.1101/2025.03.24.645039

Huang, J. & MacKerell, A. D. (2013). CHARMM36 all-atom additive protein force field: Validation based on comparison to NMR data. *J. Comp. Chem.*, *34*, 2135–2145.

Kozlowski, L. P. (2021). IPC 2.0: Prediction of isoelectric point and p*K*a dissociation constants. *Nucleic Acids Research*, *49*(W1), W285–W292. https://doi.org/10.1093/nar/gkab295

Lambalot, R. H., & Walsh, C. T. (1995). Cloning, Overproduction, and Characterization of the Escherichia coli Holo-acyl Carrier Protein Synthase (∗). *Journal of Biological Chemistry*, *270*(42), 24658–24661. https://doi.org/10.1074/jbc.270.42.24658

Li, K., Cho, Y. I., Tran, M. A., Wiedemann, C., Zhang, S., Koweek, R. S., Hoàng, N. K., Hamrick, G. S., Bowen, M. A., Kokona, B., Stallforth, P., Beld, J., Hellmich, U. A., & Charkoudian, L. K. (2025). Strategic Acyl Carrier Protein Engineering Enables Functional Type II Polyketide Synthase Reconstitution In Vitro. *ACS Chemical Biology*, *20*(1), 197–207. https://doi.org/10.1021/acschembio.4c00678

Liu, X., Hua, K., Liu, D., Wu, Z.-L., Wang, Y., Zhang, H., Deng, Z., Pfeifer, B. A., & Jiang, M. (2020). Heterologous Biosynthesis of Type II Polyketide Products Using E. coli. *ACS Chemical Biology*, *15*(5), 1177–1183. https://doi.org/10.1021/acschembio.9b00827

Madeira, F., Madhusoodanan, N., Lee, J., Eusebi, A., Niewielska, A., Tivey, A. R. N., Lopez, R., & Butcher, S. (2024). The EMBL-EBI Job Dispatcher sequence analysis tools framework in 2024. *Nucleic Acids Research*, *52*(W1), W521–W525. https://doi.org/10.1093/nar/gkae241

Marcella, A. M., Culbertson, S. J., Shogren-Knaak, M. A., & Barb, A. W. (2017). Structure, high affinity, and negative cooperativity of the Escherichia coli holo-(acyl carrier protein):holo-(acyl carrier protein) synthase complex. *Journal of Molecular Biology*, *429*(23), 3763–3775. https://doi.org/10.1016/j.jmb.2017.10.015

McBride, C. M., Miller, E. L., & Charkoudian, L. K. (2023). An updated catalogue of diverse type II polyketide synthase biosynthetic gene clusters captured from large-scale nucleotide databases. *Microbial Genomics*, *9*(3). https://doi.org/10.1099/mgen.0.000965

Nguyen, C., Haushalter, R. W., Lee, D. J., Markwick, P. R. L., Bruegger, J., Caldara-Festin, G., Finzel, K., Jackson, D. R., Ishikawa, F., O'Dowd, B., McCammon, J. A., Opella, S. J., Tsai, S. C., & Burkart, M. D. (2014). Trapping the dynamic acyl carrier protein in fatty acid biosynthesis. *Nature*, *505*, 427–431. https://doi.org/10.1038/nature12810

Pedersen, T. B., Nielsen, M. R., Kristensen, S. B., Spedtsberg, E. M. L., Sørensen, T., Petersen, C., Muff, J., Sondergaard, T. E., Nielsen, K. L., Wimmer, R., Gardiner, D. M., & Sørensen, J. L. (2022). Speed dating for enzymes! Finding the perfect phosphopantetheinyl transferase partner for your polyketide synthase. *Microbial Cell Factories*, *21*(1), 9. https://doi.org/10.1186/s12934-021-01734-9

Pettersen, E. F., Goddard, T. D., Huang, C. C., Couch, G. S., Greenblatt, D. M., Meng, E. C., & Ferrin, T. E. (2004). UCSF Chimera—A visualization system for exploratory research and analysis. *Journal of Computational Chemistry*, *25*(13), 1605–1612. https://doi.org/10.1002/jcc.20084

Pettersen, E. F., Goddard, T. D., Huang, C. C., Meng, E. C., Couch, G. S., Croll, T. I., Morris, J. H., & Ferrin, T. E. (2021). UCSF ChimeraX: Structure visualization for researchers, educators, and developers. *Protein Science*, *30*(1), 70–82. https://doi.org/10.1002/pro.3943

Pira, H., Risdian, C., Kämpfer, P., Müsken, M., Schupp, P. J., & Wink, J. (2021). Zooshikella harenae sp. Nov., Isolated from Pacific Oyster Crassostrea gigas, and Establishment of Zooshikella ganghwensis subsp. Marina subsp. Nov. And Zooshikella ganghwensis subsp. Ganghwensis subsp. Nov. *Diversity*, *13*(12), 641. https://doi.org/10.3390/d13120641

Purcell, A. W., Aguilar, M.-I., & Hearn, M. T. W. (1999). Probing the Binding Behavior and Conformational States of Globular Proteins in Reversed-Phase High-Performance Liquid Chromatography. *Analytical Chemistry*, *71*(13), 2440–2451. https://doi.org/10.1021/ac9808369

Quadri, L. E., Weinreb, P. H., Lei, M., Nakano, M. M., Zuber, P., & Walsh, C. T. (1998). Characterization of Sfp, a Bacillus subtilis phosphopantetheinyl transferase for peptidyl carrier protein domains in peptide synthetases. *Biochemistry*, *37*(6), 1585–1595. https://doi.org/10.1021/bi9719861

Robert, X., & Gouet, P. (2014). Deciphering key features in protein structures with the new ENDscript server. *Nucleic Acids Research*, *42*(W1), 320–324. https://doi.org/10.1093/nar/gku316

Sunbul, M., Marshall, N. J., Zou, Y., Zhang, K., & Yin, J. (2009). Catalytic turnover-based phage selection for engineering the substrate specificity of Sfp phosphopantetheinyl transferase. *Journal of Molecular Biology*, *387*(4), 883–898. https://doi.org/10.1016/j.jmb.2009.02.010

Sztain, T., Bartholow, T. G., Lee, D. J., Casalino, L., Mitchell, A., Young, M. A., Wang, J., McCammon, J. A., & Burkart, M. D. (2021). Decoding allosteric regulation by the acyl carrier protein. *Proceedings of the National Academy of Sciences*, *118*(16), Article 16. https://doi.org/10.1073/pnas.2025597118

Tufar, P., Rahighi, S., Kraas, F. I., Kirchner, D. K., Lohr, F. nk, Henrich, E., Köpke, J., Dikic, I., Güntert, P., Marahiel, M. A., & Dötsch, V. (2014). Crystal Structure of a PCP/Sfp Complex Reveals the Structural Basis for Carrier Protein Posttranslational Modification. *Chemistry & Biology*, *21*(4), 552–562. https://doi.org/10.1016/j.chembiol.2014.02.014

Wang, E. H., Nagarajan, Y., Carroll, F., & Schug, K. A. (2016). Reversed-phase separation parameters for intact proteins using liquid chromatography with triple quadrupole mass spectrometry: Liquid Chromatography. *Journal of Separation Science*, *39*(19), 3716–3727. https://doi.org/10.1002/jssc.201600764

Winkler, R. (2010). ESIprot: A universal tool for charge state determination and molecular weight calculation of proteins from electrospray ionization mass spectrometry data. *Rapid Commun. Mass Spectrom.*, *24*(3), 285–294. https://doi.org/10.1002/rcm.4384

Worthington, A. S., Hur, G. H., Meier, J. L., Cheng, Q., Moore, B. S., & Burkart, M. D. (2008). Probing the compatibility of type II ketosynthase-carrier protein partners. *Chembiochem*, *9*(13), 2096–2103. https://doi.org/10.1002/cbic.200800198

Worthington, A. S., Porter, D. F., & Burkart, M. D. (2010). Mechanism-based crosslinking as a gauge for functional interaction of modular synthases. *Organic & Biomolecular Chemistry*, *8*(8), 1769–1769. https://doi.org/10.1039/b925966j

Ye, Z., & Williams, G. J. (2014). Mapping a ketosynthase:acyl carrier protein binding interface via unnatural amino acid-mediated photo-cross-linking. *Biochemistry*, *53*, 7494–7502. https://doi.org/10.1021/bi500936u

Zheng, Y., Wang, C., Sakai, Y., Abe, K., Yokota, A., & Yabe, S. (2020). Dictyobacter vulcani sp. Nov., belonging to the class Ktedonobacteria, isolated from soil of the Mt Zao volcano. *International Journal of Systematic and Evolutionary Microbiology*, *70*(3), Article 3. https://doi.org/10.1099/ijsem.0.003975